

Weierstraß-Institut
für Angewandte Analysis und Stochastik
Leibniz-Institut im Forschungsverbund Berlin e. V.

Preprint

ISSN 2198-5855

Liquid-liquid dewetting: Morphologies and rates

Stefan Bommer¹, Ralf Seemann¹, Sebastian Jachalski², Dirk Peschka²,

Barbara Wagner²

submitted: December 05, 2016

¹ Experimental Physics
Saarland University
66123 Saarbrücken
Germany

E-Mail: r.seemann@physik.uni-saarland.de,
stefan.bommer@physik.uni-saarland.de

² Weierstrass Institute
Mohrenstr. 39
10117 Berlin
Germany

E-Mail: dirk.peschka@wias-berlin.de
barbara.wagner@wias-berlin.de

No. 2346

Berlin 2016



2010 *Mathematics Subject Classification.* 68.05.Cf, 02.60.Cb.

Key words and phrases. Free boundary problems, interface dynamics, experimental methods, numerical simulations.

This research was carried out in the framework of SPP5016 *Transport processes at fluidic interfaces.*

Edited by
Weierstraß-Institut für Angewandte Analysis und Stochastik (WIAS)
Leibniz-Institut im Forschungsverbund Berlin e. V.
Mohrenstraße 39
10117 Berlin
Germany

Fax: +49 30 20372-303
E-Mail: preprint@wias-berlin.de
World Wide Web: <http://www.wias-berlin.de/>

Abstract

The dependence of the dissipation on the local details of the flow field of a liquid polymer film dewetting from a liquid polymer substrate is shown, solving the free boundary problem for a two-layer liquid system. As a key result we show that the dewetting rates of such a liquid bi-layer system can *not* be described by a single power law but shows transient behaviour of the rates, changing from increasing to decreasing behaviour. The theoretical predictions on the evolution of morphology and rates of the free surfaces and free interfaces are compared to measurements of the evolution of the polystyrene(PS)-air, the polymethyl methacrylate (PMMA)-air and the PS-PMMA interfaces using *in situ* atomic force microscopy (AFM), and they show excellent agreement.

1 Introduction

Wetting and dewetting phenomena are omnipresent in nature and in technological applications and have been studied extensively for flows over flat solid substrates, e.g. [4, 16]. However, since liquid substrates are less influenced by substrate heterogeneities, it is surprising that the a similar in-depth understanding has not been reached yet for dewetting from liquid substrates. An equilibrium droplet resting on a liquid substrate deforms its support so that both components of the interfacial tension balance at the contact line and the Neumann triangle construction [15] leads to lens-shaped droplets. Away from equilibrium, a negative spreading parameter $S = \gamma_s - (\gamma_l + \gamma_{l,s})$ makes it energetically advantageous for a liquid layer to retract from the substrate and decrease its interfacial area with the underlying substrate. The resulting flow in the dewetting liquid couples to a flow in the liquid substrate and strongly influences the observed interface shapes, the flow fields and the overall dynamics of the process.

Pioneering works for the theory of liquid-liquid dewetting by Joanny [10] and Brochard-Wyart et al. [2] made predictions for small equilibrium contact angles and for the limiting regimes, where both viscosities differ by orders of magnitude. More recently the liquid-liquid dewetting was also studied using thin-film models studying different modes of instability of dewetting using simulations and stability analysis [6, 18] and also the approach of stationary states [3]. Dewetting of different liquid-liquid model systems has been studied experimentally by the group of Krausch [12, 21] for different film heights and substrate viscosities. Pan et al. [17] performed similar studies of dewetting rates and interface shapes for more viscous substrates and various substrate thicknesses. Unfortunately, none of the above works performs a comparison of experimental observed shapes with theoretical predicted ones. This seems highly relevant since the observed shapes differ considerably from the empirical predictions used to derive dewetting rates. Therefore, in this study we present a detailed comparison of experimentally obtained rim shapes, their evolution, and their dewetting dynamics with those computed from thin-film equations. Additionally, we examine the underlying mechanisms by discussing flow fields and dissipation mechanisms.

2 Experimental Methods

We consider the model system of short-chained liquid PS (ℓ) and liquid substrate PMMA (s). For the liquid-liquid dewetting experiments, thin rectangular PS patches of constant thickness $\bar{h} = h(t = 0, x, y)$ were prepared in their glassy state on top of thin glassy PMMA films of constant thickness $\bar{h}_1 = h_1(t = 0, x, y)$ supported by silicon wafers at $z = 0$. The process is started by heating the materials above the glass transition temperature and then monitored by *in situ* AFM (see Fig. 1).

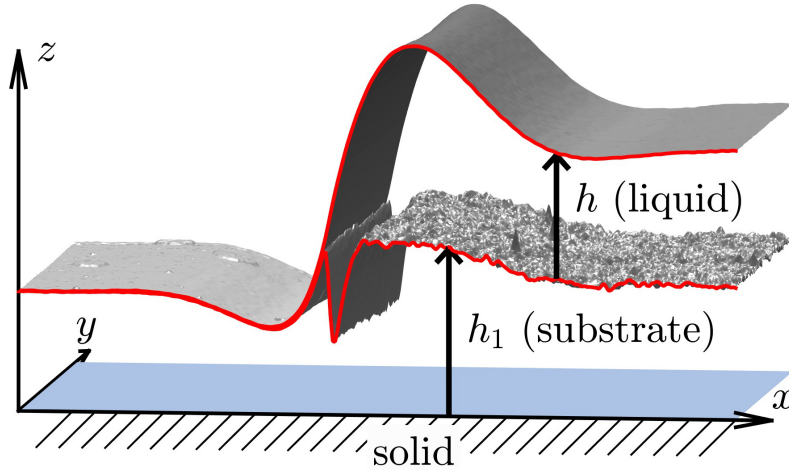


Figure 1: Composed AFM scan for 1:1 dewetting after 24 h

Therefore, silicon rectangles of about 2cm^2 were cut from $5''$ -wafers with $\langle 100 \rangle$ orientation. These silicon rectangles were pre-cleaned by a fast CO_2 -stream (snow-jet, Tectra) and sonicated in ethanol, acetone and toluene followed by a bath in peroxymonosulfuric acid (piranha etch) and a careful rinse with hot MilliporeTM water. After this cleaning procedure PMMA films were spun from toluene solution on top of the silicon support with homogeneous thicknesses. The PS films can not be spun directly onto the PMMA and were, in a first step, spun from toluene solution onto freshly cleaved mica sheets. In a second step, the glassy PS films were transferred from mica onto a MilliporeTM water surface and picked up from above with the PMMA coated silicon substrates. During this process the initially closed PS film ruptures into the aforementioned rectangular patches, which are then transferred onto the PMMA substrate. The typical film-thicknesses \bar{h}, \bar{h}_1 used in our dewetting experiments range from 50 nm to 240 nm and experiments with various ratios $\bar{h}:\bar{h}_1$ were performed.

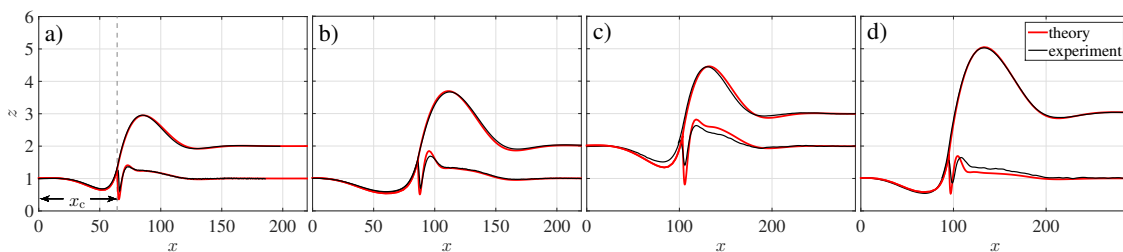


Figure 2: Interfaces from theory (red) and experiment (black) for different aspect ratios and times. Experimental cross sections are averaged over 30 scan lines of a straight front. a) 1:1 early b) 1:1 late c) 1:2 d) 2:1.

Both polymers were purchased from Polymer Standard Service Mainz (PSS-Mainz, Germany) with polydispersity of $M_w/M_n = 1.05$ and molecular weights of $M_w = 64 \text{ kg/mol}$ and $M_w = 9.9 \text{ kg/mol}$ for PS and PMMA, respectively. The dewetting experiments were conducted at a temperature of $T = 140^\circ\text{C}$ resulting in viscosities of PS $\mu_\ell \approx 700 \text{ kPa}\cdot\text{s}$ and PMMA $\mu_s = 675 \text{ kPa}\cdot\text{s}$. The viscosity values were measured using the self-similarity in stepped polymer films as presented in [14] and [20]. While errors of most experimental parameters lie within a few percent, the temperature and chain-length dependence of the polymer viscosity represents the main source of uncertainty. It easily affects the timescale of experiments and simulations within several ten percent. When matching experimental and numerical timescales we found that setting $\mu_\ell = 1100 \text{ kPa}\cdot\text{s}$ and keeping the viscosity ratio fixed gives a very good agreement for all the experiments considered. Combining the viscosities, literature values from [7, 13] and typical shear rates we estimate the Weissenberg number of order 10^{-3} , suggesting that PS and PMMA are not viscoelastic and can be considered Newtonian. Following the procedure described in [1] we experimentally determined the involved surface tensions to $\gamma_\ell = 32.3 \text{ mN/m}$, $\gamma_s = 32 \text{ mN/m}$ and $\gamma_{\ell,s} = 1.2 \pm 0.1 \text{ mN/m}$, compatible with values reported in literature, e.g. [22]. To obtain the shape of the embedded liquid-liquid interface, the dewetting process is stopped by quenching the sample down to room temperature. The now glassy samples were dipped into a selective solvent (cyclohexane, Sigma Aldrich, Germany) to remove the PS from the underlying PMMA. After drying the sample, the formerly buried PS/PMMA interface can be imaged by AFM. The full final shape of the dewetting is obtained by composing the subsequently imaged polymer/air and PS/PMMA surfaces (see FIG. 1, ¹).

3 Thin-film model

The flow describing the dewetting process is modelled by the Stokes equation $\nabla \cdot (-p_i \mathbb{I} + \mu_i(\nabla \mathbf{u}_i + \nabla \mathbf{u}_i^T)) = \mathbf{0}$ and $\nabla \cdot \mathbf{u}_i = 0$ solved in Ω_i for $i \in \{s, \ell\}$ in the substrate and the liquid. Assuming translational invariance of the 3D flow in y -direction, one can parametrize the domains

$$\Omega_s(t) = \{(x, z) \in \mathbb{R}^2 : 0 < z < h_1\}, \quad (3.1a)$$

$$\Omega_\ell(t) = \{(x, z) \in \mathbb{R}^2 : h_1 < z < h_1 + h\}, \quad (3.1b)$$

using non-negative functions $h_1(t, x), h(t, x)$ as sketched in FIG. 1. The velocity, pressure, and viscosity in Ω_i are denoted by \mathbf{u}_i, p_i, μ_i . The equations in the two regions are coupled by interface/boundary conditions, e.g. no-slip $\mathbf{u}_s = \mathbf{0}$ at $z = 0$, continuity $\mathbf{u}_\ell = \mathbf{u}_s$ at $z = h_1$ and the usual tangential and normal stress jump condition at the free interfaces $z = h_1$ and $z = h_1 + h$. Kinematic conditions relate the velocities of the flow to the velocities of surfaces and interfaces. At the contact line one needs to impose further conditions using the Neumann triangle. The equations are rescaled using

$$[z] = [x] = H, \quad [t] = H\mu_\ell/\gamma_s, \quad (3.2)$$

and replace the dimensional parameters by $\tilde{\gamma}_s = 1, \tilde{\gamma}_\ell = \gamma_\ell/\gamma_s, \tilde{\gamma}_{s,\ell} = \gamma_{s,\ell}/\gamma_s$, and $\tilde{S} = S/\gamma_s$.² Following the standard thin-film approximation we assume that the interfaces are shallow

¹**Note:** The *composition* requires rotation, shift and possibly a tilt of upper and lower AFM scan for a perfect match. Cross sections are averaged over a few scan lines.

²**Note:** We consistently normalized all experimental and numerical lengths by setting H to the initial film height so that in particular $\bar{h} = 1$.

$|\partial_x h_1|, |\partial_x h| \ll 1$. Then a formal asymptotic calculation shows that h_1, h are solutions of a system of parabolic equations defined separately on the wetted region $\omega(t) = \{x \in \mathbb{R} : h(t, x) > 0\}$ and its complement. For $x \in \omega$ we have

$$\partial_t h_1 = \partial_x (M_{11} \partial_x \pi_1 + M_{12} \pi_2), \quad (3.3a)$$

$$\partial_t h = \partial_x (M_{21} \partial_x \pi_1 + M_{22} \pi_2), \quad (3.3b)$$

with mobility matrix

$$M = \frac{1}{\mu} \begin{pmatrix} \frac{1}{3} h_1^3 & \frac{1}{2} h_1^2 h \\ \frac{1}{2} h_1^2 h & \frac{\mu}{3} h^3 + h_1 h^2 \end{pmatrix}, \quad (3.3c)$$

pressures $\pi_1 = -(\tilde{\gamma}_{\ell,s} + \tilde{\gamma}_\ell) \partial_{xx} h_1 - \tilde{\gamma}_\ell \partial_{xx} h$ and $\pi_2 = -\tilde{\gamma}_\ell \partial_{xx} h_1 - \tilde{\gamma}_\ell \partial_{xx} h$, and viscosity ratio $\mu = \mu_s / \mu_\ell$. On the complement of ω , only h_1 is unknown and solves $\partial_t h_1 = \partial_x (m \partial_x \pi_1)$ with $m = \frac{1}{3\mu} h_1^3$ and pressure $\pi_1 = -(\tilde{\gamma}_{\ell,s} + \tilde{\gamma}_\ell) \partial_{xx} h_1$. Additionally boundary conditions need to be imposed at the contact line $x_c = \partial\omega$. Note that once the solution is known, then from the thin-film approximation one can reconstruct the horizontal component of the velocity $u_i = \mathbf{u}_i \cdot \hat{\mathbf{x}}$ using

$$u_s = \frac{\partial_x \pi_1}{2\mu} z^2 + c_{s,1} z + c_{s,2}, \quad (3.4a)$$

$$u_\ell = \frac{\partial_x \pi_2}{2} z^2 + c_{\ell,1} z + c_{\ell,2}, \quad (3.4b)$$

for $x \in \omega$. The functions $c_{s,1}, c_{s,2}, c_{\ell,1}, c_{\ell,2}$ depend on (t, x) and are determined using the boundary conditions $u_s = 0$ at $z = 0$, $u_s - u_\ell = \partial_z(u_s - \mu u_\ell) = 0$ at $z = h_1$, $\partial_z u_\ell = 0$ at $z = h_1 + h$ as before. The velocity in the complement is determined analogously. The derivation of this model can be found in [9, 11, 19] and the corresponding novel numerical method is described in [8].

4 Comparison of interface morphology and rates

In Figs. 2a-d) we show the perfect alignment of the experimentally measured and theoretically computed interface profiles. One can observe features, that to some extent have been reported previously. The contact line is elevated by the flow, a dynamic feature not observed in stationary droplets for sufficiently thick substrates [1]. The material of the dewetting liquid (PS) accumulates in a rim which, by conservation of mass, grows in time when the liquid retracts from the substrate. Also some material of the substrate (PMMA) is dragged along generating a depletion near $x < x_c$ and an accumulation of substrate material near $x > x_c$. Right next to the contact line, some part of the dewetting liquid extends deeply into the substrate and generates a trench and thereby produces additional resistance against the dewetting motion. Note that the size of the trench does not or only depends weakly on size size of the dewetting rim. Compared to the aspect ratio 1:1 in Fig. 2a), switching aspect ratios has no influence on the qualitative behavior of solutions and the perfect match between experiment and simulation. The only influence is that for thicker substrates 1:2 Fig. 2c) these features grow and for thinner substrates 2:1 Fig. 2d) these features shrink in size. Away from the rim the interfaces decay in an oscillatory fashion into their prepared constant states $h_1(t, x), h(t, x) \rightarrow \bar{h}_1, \bar{h}$.

For a fixed aspect ratio (3.2) predicts that, due to the absence of additional intrinsic time and length scales for Newtonian liquids, the influence of the absolute height is to scale time linearly

with no change in the rescaled heights. In order to check this hypothesis two samples with aspect ratio 1:1 but film thicknesses $\bar{h} \approx 100$ nm and $\bar{h} \approx 240$ nm were prepared and are shown in FIG. 3. This confirms previously made assumption and shows the reproducibility of the experiment.

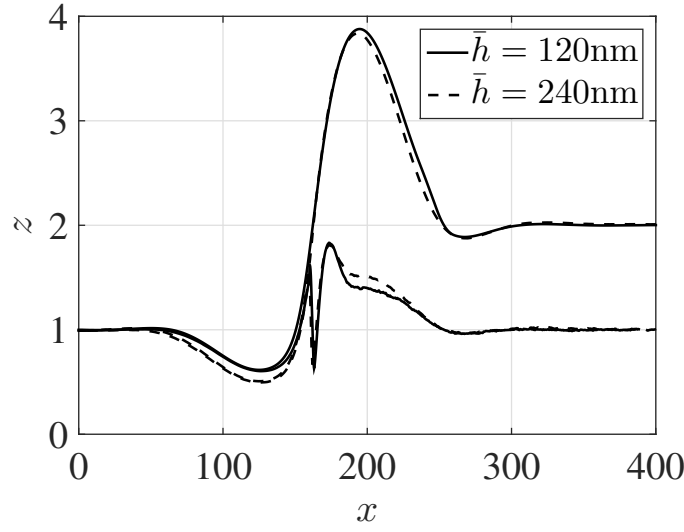


Figure 3: Experiments with 1:1 and $\bar{h} = 120, 240$ nm.

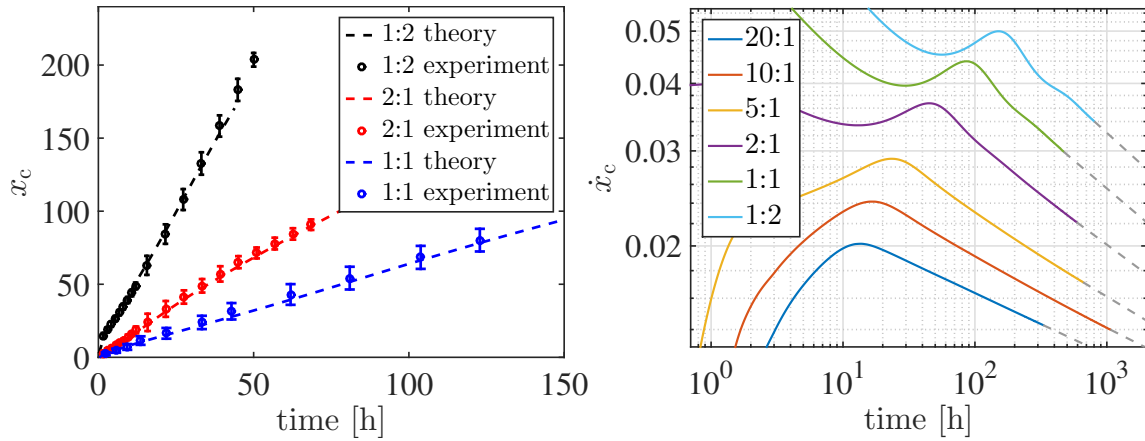


Figure 4: (left) Dewetted distance x_c for aspect ratios 1:1 (240nm:240nm), 2:1 (90nm:45nm), 1:2 (45nm:90nm) from experiment (circles with error) and simulation (dashed lines) suggesting constant dewetting rates $\dot{x}_{c,1:1} = 4.4 \times 10^{-2}$ nm/s, $\dot{x}_{c,2:1} = 3 \times 10^{-2}$ nm/s, $\dot{x}_{c,1:2} = 5.2 \times 10^{-2}$ nm/s, where (right) longer simulations prove that rates \dot{x}_c decrease depending on the aspect ratio (gray dashed lines guide the eye)

Also the experimental contact line dynamics, i.e. x_c as a function of time, is perfectly reproduced by the thin-film model for various aspect ratios, see Fig. 4 (left). The dewetting rate appears linear $x_c \sim t$, however, there is no theoretical indication whatsoever that for aspect ratios and viscosity ratios of order one there should be a power-law dewetting rate. Also, a closer inspection of the rates in Fig. 4 (left) and further simulation for other aspect ratios in Fig. 4 (right) proves that the velocity slowly decreases over time with transient rates depending on the aspect ratio at hand, i.e. $\dot{x}_c \sim t^{-0.22}$ for 1:2 and $\dot{x}_c \sim t^{-0.11}$ for 20:1. This also confirms previous speculations by Krausch et al. [12] about the transient nature of the observed dewetting dynamics.

Since the thin-film model accurately predicts shapes and speeds of the liquid-liquid dewetting, we extend this approach and discuss flow features that otherwise would be inaccessible for measurements. For instance, the dissipation is in balance with the driving surface tension

$$\int_{\Omega_1} \frac{1}{2} (\partial_z u_s)^2 d\Omega + \int_{\Omega_2} \frac{\mu}{2} (\partial_z u_\ell)^2 d\Omega = (-S) \dot{x}_c, \quad (4.1)$$

and thereby shows where the materials offer resistance to the flow. While the driving force is relatively easy to understand, the dissipation depends on local details of the flow field. For a typical layer aspect ratio 1:1 we show rim profiles overlaid with the dominating horizontal component of the velocity in FIG. 5 (top) and the corresponding dissipation $(\partial_z u_\ell)^2$ and $\mu(\partial_z u_s)^2$ (bottom), the latter on a logarithmic scale. The bottom panel of Fig. 5 shows there are substantial contributions to the dissipation from both the liquid and the substrate. Only for the equal viscosities considered here, the velocity field smoothly extends from the free liquid-air interface to the substrate-solid interface leading to a continuous dissipation. At the solid interface at $z = 0$ and remote from the rim $|x - x_c| \gg 0$ the velocity field and the dissipation vanishes. Due to the boundary conditions $\partial_z u_{s,\ell} = 0$ the dissipation also vanishes at the liquid/air and substrate/air interface. The velocity points mainly in the positive x -direction with its maximum at the contact line. However, there is also a rather strong and localized backflow in the liquid substrate below the depression of the liquid-substrate interface. This backflow is due to conservation of mass balancing the forward transport of the upper depression. There and close to

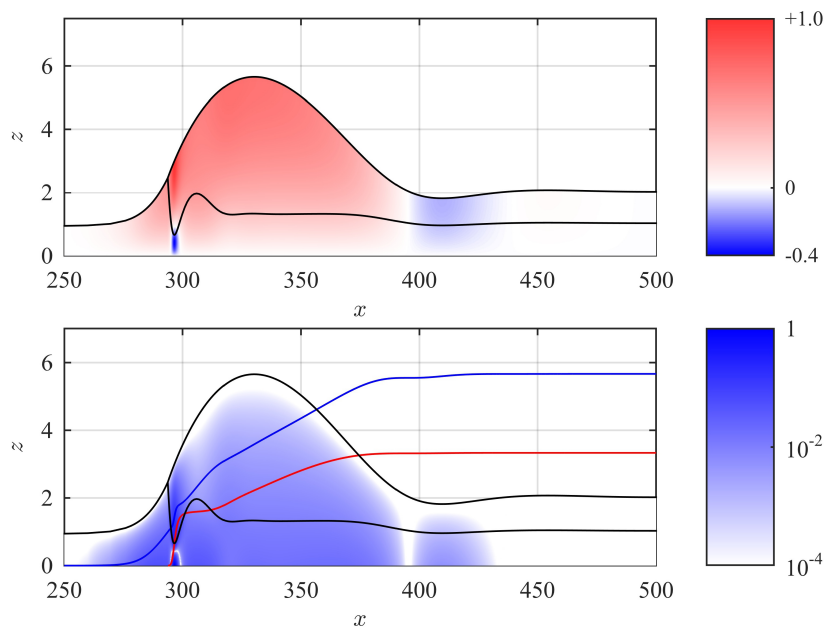


Figure 5: (top) velocities u_s, u_ℓ computed from (3.4) and (bottom) corresponding dissipation $D_s = (\partial_z u_s)^2$ and $D_\ell = \mu(\partial_z u_\ell)^2$ on logarithmic scale normalized to their respective maximal values during dewetting with aspect ratio 1:1. The additional colored curves indicate the cumulative dissipation in substrate $\int_0^x \int_0^{h_1} D_s dz dx$ (blue) and liquid $\int_{h_1}^{h_1+h} \int_0^x D_\ell dz dx$ (red) in arbitrary units.

the contact line the maximal dissipation (density) is reached. However, due to the small size of these regions the integrated dissipation near contact line and in the remaining rim are of the same order. To emphasize this fact, we also plot the cumulative dissipation in the lower panel of FIG. 5. Since the shear rate is largest at the solid interface where $z = 0$, clearly the dissipation for an aspect ratio 1:1 is larger in the substrate for the short and moderate times considered

experimentally. However, with the volume of the liquid layer increasing in time, ultimately the dissipation in the liquid layer will dominate for large times or for higher aspect ratios. Similarly, one can identify two different zones where the dissipation is generated. First, the cumulative dissipation shows that about $1/3$ the dissipation is produced in a small region near the contact line, i.e. $290 < x < 310$. This is visible in the relatively steep increase in the dissipation in that area. Second, the remaining contribution to the dissipation is more or less evenly distributed over the rim width resulting in a moderate and constant increase of the cumulative dissipation over the width of the rim.

5 Conclusion

The power-law dewetting rates predicted by Brochard et al. [2], however, rely the assumption that the total dissipation is generated in one such localized zone together with a nearly self-similar growth of rim shapes. On solid substrates, for instance, in the intermediate slip model [5] the dominant contribution comes from a substrate dissipation, so that the total dissipation is proportional to the rim width and the squared dewetting velocity leading to a $x_c \sim t^{2/3}$ dewetting law. Another example from the above reference is the no-slip model with a regularization, where the dissipation is localized near the contact line and thereby one obtains a linear dewetting law $x_c \sim t$ with logarithmic corrections. However, the above consideration show the dewetting process is in no regime that admits a suitable simplification to a power-law rate. In conclusion, the observed patterns and rates result from a complex interaction of substrate and liquid flow and are of transient nature. At large times, beyond experimental reach, the velocities decrease slowly without an universal exponent or dominating mechanism. Thin-film models are adequate to describe features and make detailed quantitative predictions about AFM measurements of the dewetting process.

References

- [1] S. Bommer, F. Cartellier, S. Jachalski, D. Peschka, R. Seemann, and B. Wagner. Droplets on liquids and their journey into equilibrium. *The European Physical Journal E*, 36(8):1–10, 2013.
- [2] F. Brochard-Wyart, P. Martin, and C. Redon. Liquid/liquid dewetting. *Langmuir*, 9(12):3682–3690, 1993.
- [3] R.V. Craster and O.K. Matar. On the dynamics of liquid lenses. *Journal of Colloid and Interface Science*, 303(2):503–516, 2006.
- [4] P.G. de Gennes, F. Brochard-Wyart, and D. Quéré. *Capillarity and wetting phenomena: drops, bubbles, pearls, waves*. Springer, 2004.
- [5] R. Fetzer, K. Jacobs, A. Münch, B. Wagner, and T.P. Witelski. New slip regimes and the shape of dewetting thin liquid films. *Physical Review Letters*, 95(12):127801, 2005.
- [6] L.S. Fisher and A.A. Golovin. Nonlinear stability analysis of a two-layer thin liquid film: Dewetting and autophobic behavior. *Journal of Colloid and Interface Science*, 291(2):515–528, 2005.

- [7] Y. Hirai, T. Yoshikawa, N. Takagi, S. Yoshida, and K. Yamamoto. Mechanical properties of poly-methyl methacrylate (PMMA) for nano imprint lithography. *Journal of Photopolymer Science and Technology*, 16(4):615–620, 2003.
- [8] R. Huth, S. Jachalski, G. Kitavtsev, and D. Peschka. Gradient flow perspective on thin-film bilayer flows. *Journal of Engineering Mathematics*, 94(1):43–61, 2015.
- [9] S. Jachalski, D. Peschka, A. Münch, and B. Wagner. Impact of interfacial slip on the stability of liquid two-layer polymer films. *J. Engr. Math.*, 86(1):9–29, 2014.
- [10] J.F. Joanny. Wetting of a liquid substrate. *Physicochemical Hydrodynamics*, 9(1-2):183–196, 1987.
- [11] J.J. Kriegsmann and M.J. Miksis. Steady motion of a drop along a liquid interface. *SIAM Journal on Applied Mathematics*, 64(1):18–40, 2003.
- [12] P. Lambooy, K.C. Phelan, O. Haugg, and G. Krausch. Dewetting at the liquid-liquid interface. *Physical Review Letters*, 76(7):1110, 1996.
- [13] P. Lomellini. Effect of chain length on the network modulus and entanglement. *Polymer*, 33(6):1255–1260, 1992.
- [14] J.D. McGraw, T. Salez, O. Bäümchen, E. Raphaël, and K. Dalnoki-Veress. Self-similarity and energy dissipation in stepped polymer films. *Physical Review Letters*, 109(12):128303, 2012.
- [15] F.E. Neumann. *Vorlesungen über mathematische Physik: Vorlesungen über die Theorie der Capillarität*, volume 7. BG Teubner, 1894.
- [16] A. Oron, S.H. Davis, and S.G. Bankoff. Long-scale evolution of thin liquid films. *Reviews of Modern Physics*, 69(3):931, 1997.
- [17] Q. Pan, K.I. Winey, H.H. Hu, and R.J. Composto. Unstable polymer bilayers. 2. The effect of film thickness. *Langmuir*, 13(6):1758–1766, 1997.
- [18] A. Pototsky, M. Bestehorn, D. Merkt, and U. Thiele. Alternative pathways of dewetting for a thin liquid two-layer film. *Physical Review E*, 70(2):025201, 2004.
- [19] A. Pototsky, M. Bestehorn, D. Merkt, and U. Thiele. Morphology changes in the evolution of liquid two-layer films. *The Journal of chemical physics*, 122:224711, 2005.
- [20] T. Salez, J.D. McGraw, S.L. Cormier, O. Bäümchen, K. Dalnoki-Veress, and E. Raphaël. Numerical solutions of thin-film equations for polymer flows. *The European Physical Journal E*, 35(11):1–9, 2012.
- [21] C. Wang, G. Krausch, and M. Geoghegan. Dewetting at a polymer-polymer interface: film thickness dependence. *Langmuir*, 17(20):6269–6274, 2001.
- [22] S. Wu. Surface and interfacial tensions of polymer melts. ii. poly (methyl methacrylate), poly (n-butyl methacrylate), and polystyrene. *The Journal of Physical Chemistry*, 74(3):632–638, 1970.